Synthesis of MOF-derived porous multi-metal/carbon composites by metal regulation strategy for efficient microwave absorption application

Yuting Li[1], Kun Zhang[1,2,*] , Zhizhen Xu[1], Xiaoyu Zhao[1], Yaxin Wang[1], Fengyi Zhang[1], Xiaojie Guo[1], and Yongjun Zhang[1,2,*]

[1] *School of Material and Environmental Engineering, Hangzhou Dianzi University, Hangzhou 310018, China*
[2] *Hangzhou Dianzi University Shangyu Institute of Science and Engineering, Shaoxing 312300, China*

ABSTRACT

The combination of carbon and ferrimagnet metallic materials derived from metal-organic frameworks (MOFs) have received increasing research interest for high performance electromagnetic wave absorption (EMA) materials due to their unique composition and microstructure. Here, a series of MOF-74 is synthesized by tuning the ratio of mixed metallic ions of cobalt and nickel, which are then treated in an inert atmosphere to fabricate novel composites with metallic cores encapsulated in a porous carbon shell. The dielectric loss caused by carbon shells and the magnetic loss caused by the cores of cobalt, nickel, or their alloys, coupled with the interfacial polarization caused by the space charge formed between the magnetic cores and the dielectric carbon shells, the highly efficient electromagnetic wave absorption performance of the composites is ensured. Ni@PC has a better EMA with an effective absorption bandwidth of 4.72 GHz at a thickness of 2.66 mm, while CoNi@PC_1 has an effective absorption bandwidth of 4.16 GHz at a thickness of 2.08 mm and is the thinnest at similar absorption widths. The properties obtained in this study indicate that the bimetallic MOF-74 with adjustable metal-ion ratio provides a new idea for the fabrication of high-efficiency MOF-based EMA materials.

1 Introduction

With the rapid development of telecommunications and modern electronic technologies, electronic products have permeated every aspect of our lives [1–3]. However, the adverse effects of the ensuing electromagnetic radiation, which directly affect the physical health of natural organisms and the normal operation of other electronic devices, cannot be ignored. In the face of these detrimental factors, there is an urgent need to accelerate the development of electromagnetic absorbing (EMA) materials [4–9].

Yuting Li and Kun Zhang have contributed equally to this work.

Address correspondence to E-mail: kunzhang@hdu.edu.cn; yjzhang@hdu.edu.cn

🙂 Springer

Over the past decades, much attention ha**s** been paid to the fabrication of various EMA materials based on ferromagnetic metals, carbon, conductive polymers, etc., which all exhibit preferable electromagnetic response properties when applied individually. However, they are significantly different in terms of the breadth of the application domain and the performance of the EMA due to the difference in their intrinsic properties. It can also be understood that their EMA capacity is somewhat limited in the face of harsh and complex electromagnetic environments [10–13].To the best of our knowledge, ferromagnetic metallic materials, including Fe, Ni, Co and their alloys, exhibit strong EMA properties while suffering from high density, susceptibility to corrosion, poor dielectric properties and narrow frequency ranges [14, 15]. Carbon materials exhibit superior dielectric loss properties, light weight, good chemical stability and excellent permittivity, but only the dielectric loss allows for low impedance matching [16–21]. Addressing the dilemma encountered in the development of one-component absorbing materials. Most multi-component EMA materials have been synthesized by combining the two materials, carbon materials and magnetic elements, which allows the two components to be used effectively to complement each other in terms of permittivity, permeability, and impedance matching, improving the EMA properties and increasing the absorption bandwidth [22]. However, in view of the high efficiency synergy of the recombination materials, the two components, dielectrically and magnetically, should be tightly bound and uniformly distributed [23–25] such as the construction of multilayer and core-shell structure, which can also provide abundant heterogeneous interface [26].

Metal-organic frameworks (MOFs) are crystalline materials formed by the self-assembly of metal ions with organic ligands. This material has a unique structure and is an ideal precursor for the fabrication of metal-based compounds/carbon composites [27]. Typically, MOFs can be pyrolyzed into their derivatives, including metals, monometallic oxides, polymetallic oxides [28], carbon nanotubes [29], and amorphous carbon in inert atmospheres, which are chemically stable, porous, and also exhibit excellent EMA properties [30–34]. Thus, MOFs, as precursors, show great potential in the field of EMA materials. For example, Ma et al. synthesized a novel composite with a hierarchical porous lamellar structures decorated with Co nanospheres derived from Co-MOF precursors by a solvothermal process followed by further annealing. The resulting Co/C composite shows a high saturation magnetization [35]. Wen et al. have also fabricated Ni/C nanocomposites derived from Ni-MOFs, which can effectively induce good electromagnetic wave absorption properties due to the porous and hierarchical structure resulting from the abundance of pores and multi-heterogeneous interfaces [36]. However, in the current literature, researchers mostly focus on single-metal MOF microwave absorbers and study the effect of carbonation temperature on EMA performance. In order to increase the adaptability of materials to the complex electromagnetic environments, we can improve the EMA capability by tuning the ferromagnetic metallic components. Compared to single-metal MOF derived EMA materials, multi-metal MOF composites may have a better performance in the regulation of electromagnetic parameters, which can significantly increase the variability of the magnetic response properties.

MOF-74 is an automated assembly synthesis of divalent transition metals and ligand 2,5-dimethylterephthalic acid with hexagonal honeycomb topologies, arranged with a wealth of non-coordinated unsaturated open metal sites, with organic ligand and metal ion tunability. MOF-74 can be fabricated based on different metal ions, including ferromagnetic metal ions (Co^{2+}, Fe^{2+}, Ni^{2+} etc.), forming different transition metal isomorphic structure. These features of MOF-74 provide us with a guide for the preparation of multi-metal MOF-74 based EMA materials. Moreover, Cobalt, nickel, and their alloys are considered as ideal materials for fabricating excellent EM wave absorbers due to their superior and tunable magnetic properties, resulting in better magnetic response behavior. Here, carbon/metal EMA materials have been prepared using multi-metal MOF-74 (M-MOF-74) as precursors, which are constructed by bimetallic metal of Co and Ni, and the ratio of the two metals are also tuned. For comparison, Co-MOF-74 and Ni-MOF-74 consisting of monometallic elements were also obtained. After thermal decomposition, a series of MOF-74 derivatives were prepared, including Ni/C, Co/C, Co, Ni/C composites. By analyzing the electromagnetic parameters of these composites, the effect of different components on the EMA performance can be effectively understood. The composition of magnetic metal ions plays an obvious role in modulating the electromagnetic parameters of materials, which directly determines their EMA properties. Magnetic

cobalt, nickel and their alloyed nanoparticles are uniformly dispersed in the carbon matrix, forming rich interfaces and interfacial polarizations. In addition, the combined effect of multi-component and porous structure, the efficient absorption performance of the composite after pyrolysis is guaranteed. The absorption mechanism of the single- and double-metal MOF-74 derivatives is further explored from the impedance matching properties. It is worth noting that the CoNi@PC_1 achieves a maximum effective absorption bandwidth of 4.16 GHz at a thickness of 2.08 mm, and its effective absorption ranging at 3.36- 18 GHz.

2 Experimental section

2.1 Chemical reagents

2,5-dihydroxyterephthalic acid ($C_8H_6O_6$), Cobalt Chloride Hexahydrate ($CoCl_2 \cdot 6H_2O$), Nickel Chloride Hexahydrate ($NiCl_2 \cdot 6H_2O$) were purchased from Shanghai Macklin Chemical Co., Ltd., N, N-Dimethylformamide (DMF) and Ethanol were purchased from High Crystal Chemical Co., Ltd. All chemicals were used as received without any further purification. Deionized water was used as the water source throughout this work.

2.2 Preparation of MOF-74

As reported previously [37], the bimetallic CoNi-MOF-74 was synthesized using the hydrothermal method. In brief, $CoCl_2 \cdot 6H_2O$ and $NiCl_2 \cdot 6H_2O$ were dissolved in a 60 mL mixture of deionized water, ethanol and DMF. The solvent mixture in the resulting solution is DMF:DI:EtOH = 1:1:1 vol. After that, 2,5-dihydroxyterephthalic acid was added to the above solvent mixture, and then the mixture was transferred to a 100 mL Teflon-lined autoclave and heated at a controlled temperature of 120 °C for 20 h. The precipitate was thoroughly collected via centrifugation at 5000 rpm for 5 min and further washed 3 times with DMF and 3 times with methanol. Finally, the solid product of CoNi-MOF-74 was dried at 100 °C for 12 h under vacuum. The Co/Ni molar ratios in the final mixture solution were 4:0, 1:3, 2:2, 3:1, 0:4 and the corresponding products were labeled as Co-MOF-74, CoNi-MOF-74_1 (1:3), CoNi-MOF-74_2 (2:2), CoNi-MOF-74_3 (3:1) and Ni-MOF-74, respectively.

2.3 Preparation of MOF-74 derivatives

All the synthesized MOF-74 with different molar ratios of Co and Ni were further processed under calcination. For details, a certain number of products was added to a ceramic pool, and then calcinated in argon from room temperature to 700 °C, with heating rate of 3 °C/min, and maintained for 2 h at 700 °C. After calcinations, the final products were named as Co@PC, CoNi@PC_1, CoNi@PC_2, CoNi@PC_3 and Ni@PC, which were derived from Co-MOF-74, CoNi-MOF-74_1 (1:3), CoNi-MOF-74_2 (2:2), CoNi-MOF-74_3 (3:1) and Ni-MOF-74, respectively.

2.4 Material characterization

The microstructure and morphology of the samples were characterized by field emission scanning electron microscopy (FE-SEM; JOEL/JSM-IT500HR) and transmission electron microscope (TEM; Talos F200S). The crystal structure of the sample was recorded by X-ray powder diffraction (XRD; Mini-Flex 600X). Chemical bonds and chemical states were measured by X-ray photoelectron spectroscopy (XPS; Thermo Scientific K-Alpha). The graphitization degrees were analyzed through a Raman spectrometer (Raman; HR Evo Nano). The complex permittivity and permeability of the sample were measured by a vector network analyzer (VNA; N5242A PNA-X, Agilent) in the 2–18 GHz frequency range. The toroidal-shaped ring was prepared by mixing a 30% weight sample with 70% weight paraffin wax. Using Matlab software to calculate the reflection loss (RL) curve according to the transmission theory to evaluate the absorption characteristics of electromagnetic wave. The EMW absorption properties of the five samples were evaluated according to the following formula.

3 Results and discussion

3.1 Structural and compositional analysis

The fabrication procedures of CoNi-MOF-74_1–3 and their derivatives of CoNi@PC is shown in Fig. 1. First, the two-metal ion precursors of Co^{2+} and Ni^{2+} were added to a solvent mixture of DMF/water/ethanol under a continuous stirring for 1 h, after which

Fig. 1 Schematic diagram of synthetic process for CoNi-MOF-74, and CoNi@PC
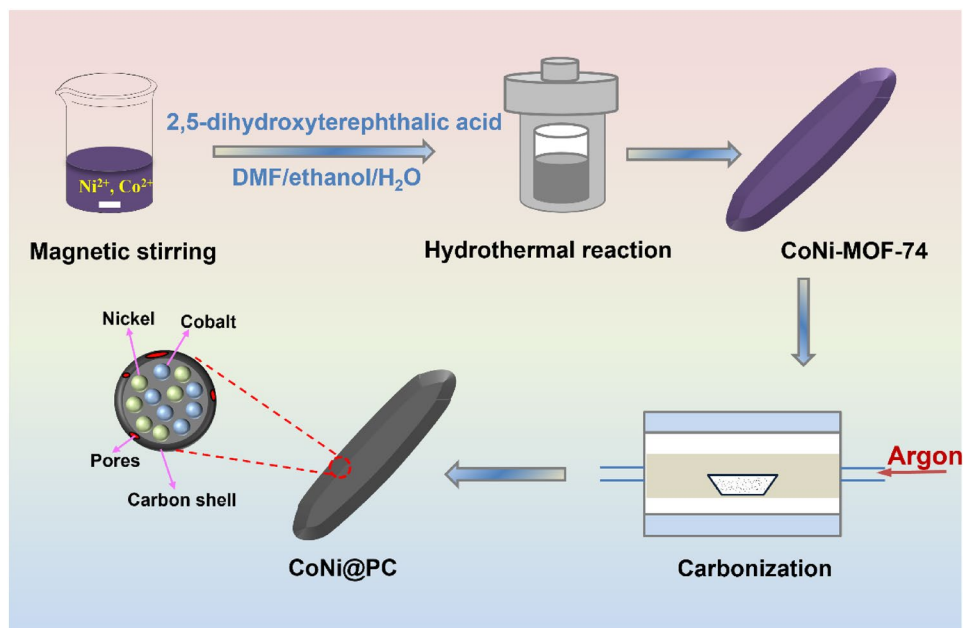
a certain amount of the organic molecule 2, 5-dihydroxyterephthalic acid was added to the above solution. Then, they were transferred to a Teflon-lined stainless-steel autoclave and incubated in 120 °C for 20 h. The bimetallic MOF-74 were formed due to the strong coordination of Co^{2+} and Ni^{2+} with 2,5-dihydroxyterephthalic acid in the high-temperature and high-pressure environment. At last, the synthesized bimetallic MOF powder was moved to a quartz tube furnace, and the temperature-controlled calcination process was carried out to prepare the bimetallic of Co and Ni loaded porous carbon (CoNi@ PC) EMA materials. To the best of our knowledge, the EMA is favored by the fact that high temperatures lead to the collapse of the MOF structure and the formation of new matters, the transfer of organic ligands to carbon, and the reduction of metal ions to their metallic or metallic oxides. According to the previous report [38], in this work, 700 °C was chosen as the optimized thermal decomposition temperature and the argon was chosen as the protective gas. The carbon wraps around the magnetic metal nanoparticles [39], forming a shell, and the combustion of the organic component results in the formation of a porous structure.

The morphological and microstructural of as-prepared MOF-74 is investigated in detail, and their scanning electron microscopy (SEM) images are presented in Fig. 2a–e. As shown in Fig. 2a, the

Co-MOF-74 crystal has the shape of an elongated rod with an average size of a few tens of microns. Whereas, by changing the Co^{2+} to Ni^{2+}, the resulting Ni-MOF-74 crystal is in a typical flower-like structure with a relatively uniform size within a few microns. The different molar ratios of Co^{2+} and Ni^{2+} are of great importance in the morphological evolution, Fig. 2c–e show the SEM images of the crystals prepared with different Co/Ni molar ratios. At the ratio of Co^{2+}:Ni^{2+} of 1:3, CoNi-MOF-74_1 is presented in the form of large crystalline particles, when the ratio changes to 2:2 and the morphology of CoNi-MOF-74_2 gradually develops a structure of multiple nanorods crossing each other with an inhomogeneous size distribution, while as the ratio of Co^{2+}:Ni^{2+} further increased to 3:1, CoNi-MOF-74_3 inherits the rod-like structure of Co-MOF-74 and some nanoparticles are aggregated on the surface. Therefore, it can be concluded that the morphology of MOF-74 is significantly affected by the ratio of the constituent metal ion precursors. It is well known that the morphological evolution of MOF is largely influenced by the reaction solvent, temperature, metal precursors, and the type of organic components etc. Here, all the samples were synthesized in the same environment, so the difference in the morphology of the fabricated MOF-74 samples mainly arise from the different composition of the metal-oxygen clusters, which may result from the different sizes of metallic ions of Co^{2+} and Ni^{2+}. For CoNi-MOF-74_1
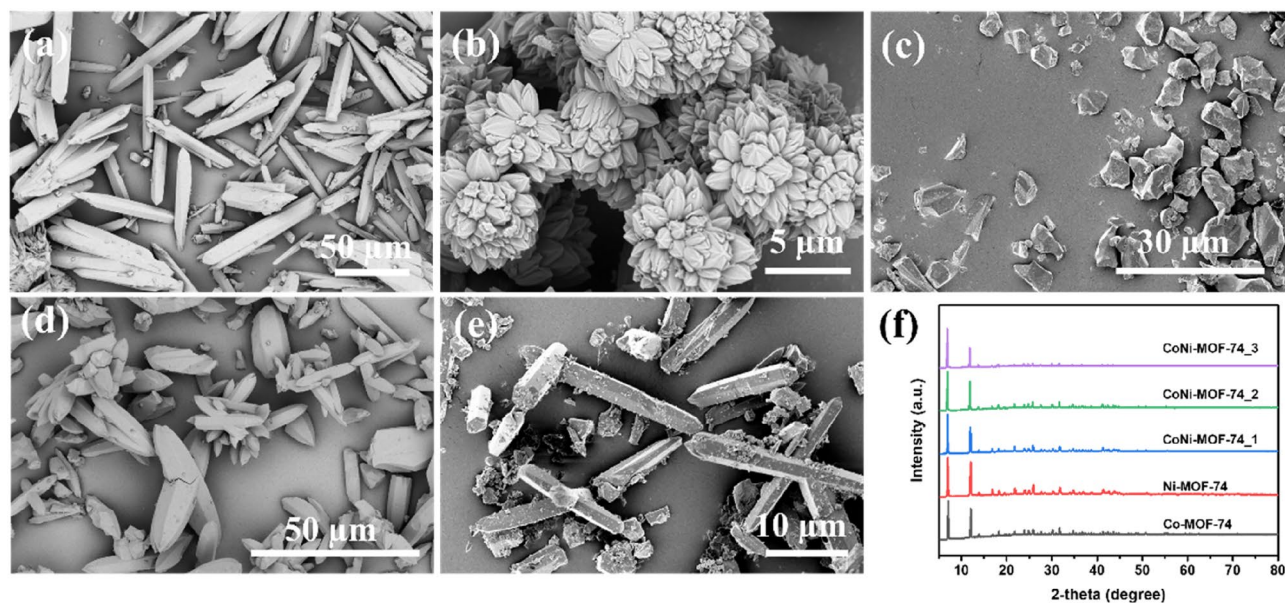
Fig. 2 SEM images of Co-MOF-74 (**a**), Ni-MOF-74 (**b**), CoNi-MOF-74_1 (**c**), CoNi-MOF-74_2 (**d**), CoNi-MOF-74_3 (**e**), and XRD pattern of all the synthesized MOF-74 (**f**)

and 3, the metal-oxygen clusters of MOF-74 are formed by bimetal ions of different sizes and with more in-equable metal molar ratios, and the asymmetry in the microstructure of metal-oxygen clusters will cause the incomplete macroscopic structure of MOF-74, leading to the breakage of the rod-like structure of MOF-74 (Fig. 2c and e). In contrast to CoNi-MOF-74_2 is formed from equivalent metallic molar ratios, resulting in a relatively unbroken morphological structure (Fig. 2d). These further indicate that the two metal ions are jointly and evenly involved in the construction of the polymetallic MOF-74. The homogeneous periodicity of single or bimetallic oxygen clusters not only regulates the microstructure of the MOF-74, but is also a prerequisite for the uniform dispersion and tight binding of the metal/carbon components in their pyrolytic derivatives, and thus further facilitates the exertion of magnetic/dielectric synergies and the formation of multiple interfaces. The powder X-ray diffraction (PXRD) analysis was carried out to identify the structure and composition of the samples. Figure 2f shows the PXRD patterns of Co-MOF-74, Ni-MOF-74, and CoNi-MOF-74_1–3. All the prepared MOF-74s have the diffraction peaks at the same 2-theta position, particularly exhibited by two intense characteristic peaks at 2-theta values of 7.1 and 12, indicating the same crystalline structure despite their morphological differences. The XRD pattern of Co-MOF-74 is consistent with that reported in previous reports [40], confirming the successful synthesis of Co-MOF-74. The patterns of Ni-MOF-74 and CoNi-MOF-74_1–3 are consistent with that of Co-MOF-74, demonstrating that mixed metal ions with different ratios can coexist well in the newly synthesized crystals.

After calcination in argon, powder XRD tests were performed to determine the structure and composition of the samples. As shown in Fig. 3a, there is a broad peak shown in each XRD pattern of the prepared sample at the 2θ range of 20°–25° with relatively low intensity, which is attributed to the carbonization of organic components to amorphous carbon. The Co@PC sample featured diffraction peaks at 44.22°, 51.53°, and 75.86°, corresponding to the (111), (200), and (220) planes of cobalt phase (PDF # 04-005-9456). The appearance of these peaks validates the successful in-situ formation of metallic cobalt from Co^{2+} reduction under current conditions. The Ni@PC sample featured three diffraction peaks at 44.41°, 51.75°, and 76.22°, corresponding to the (111), (200), and (220) planes of nickel phase (PDF # 04-002-7521), which are located at the similar 2θ positions with metallic cobalt phase. However, there are two additional well-resolved peaks at 41.95° and 44.26° existed in the as synthesized Ni@PC XRD pattern, which can be assigned to the (100) and (002) planes of another crystal phase of metallic nickel (PDF # 97-067-1412). All these diffraction peaks verify the

Fig. 3 PXRD patterns **a** of
Co@PC, Ni@PC and CoNi@
PC_1-3, XPS survey scan
spectra **b** of CoNi@PC_1-3,
and the high-resolution spec-
trum of C 1s (**b**), Co 2p **d**
and Ni 2p **e** of CoNi@PC_1,
Raman spectra (**f**) and room-
temperature hysteresis loops
g and **h** of Co@PC, Ni@PC
and CoNi@PC_1-3
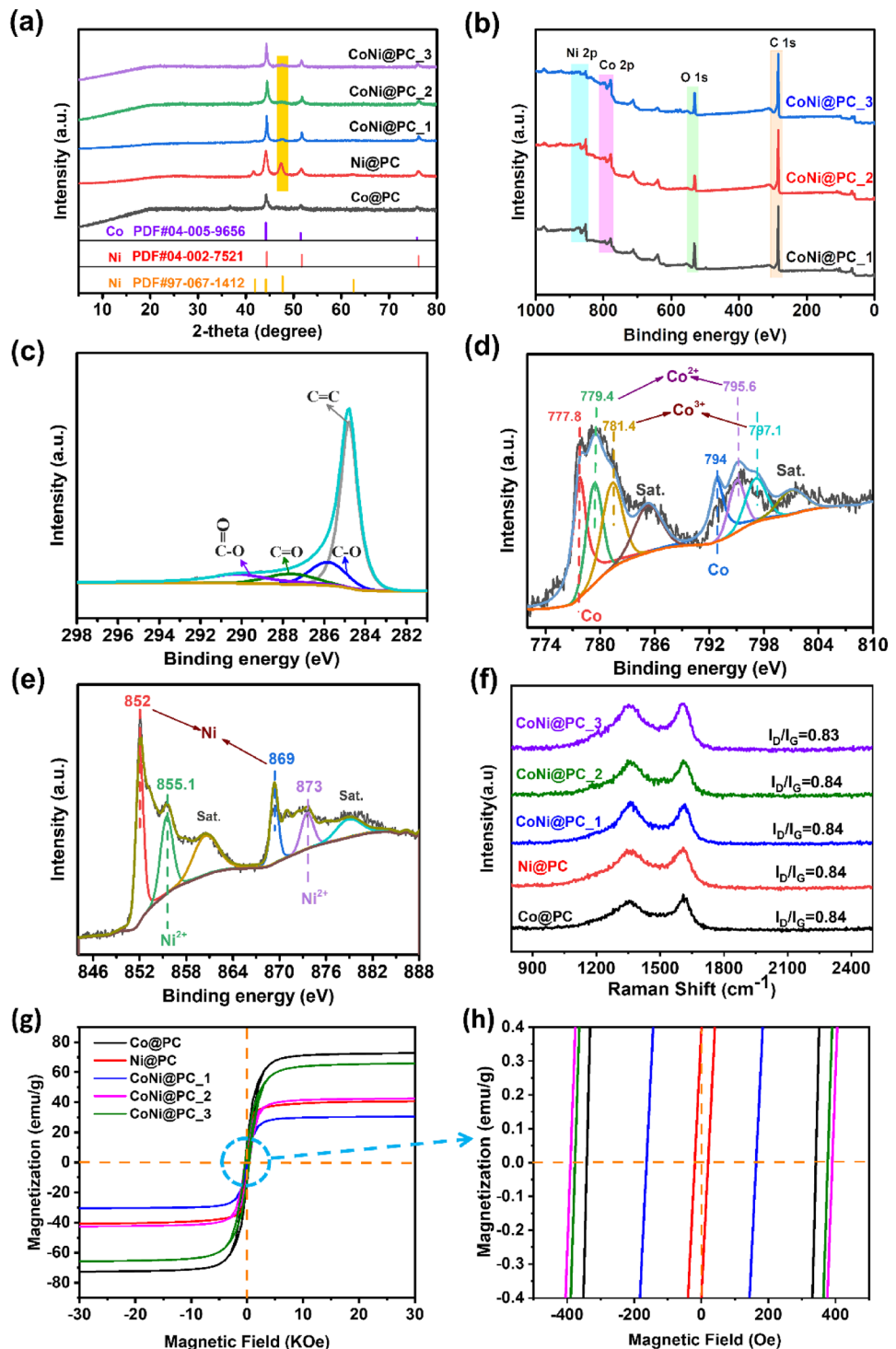
reduction of Ni^{2+} into two metallic nickel phases. The three well-resolved diffraction peaks appearing in the XRD patterns of the three composites of CoNi@PC_1-3 with the same 2θ positions, which may come from the superposition of diffraction peaks of metallic cobalt and nickel. Additionally, the metallic nickel phase with (002) plane (label as orange shaded area in Fig. 3a) can also be detected in CoNi@PC_1-3 with relatively weak intensity in their peaks, and the peak intensity gradually decreased with increase the ratio

of Co^{2+} and Ni^{2+}, indicating that the contents of metal ions in the synthesized samples are strictly affected by the feeding ratio.

The chemical composition and valence state of the surface elements of the calcined products were analyzed by XPS measurements. Figure 3c shows the XPS survey scan spectrum of CoNi@PC_1-3, revealing the existence of C, O, Co, and Ni elements in the three composites. The C 1s peak is attributed to the graphite carbon and O 1s mainly comes from the carboxyl group of organic ligands. For CoNi@PC_1, the high-resolution C1s spectrum (Fig. 3d) has four diffraction peaks at 284.6 eV, 285.7 eV, 288.7 eV, and 290.4 eV, which correspond to C=C, C–O, C=O, and O=C–O, respectively, demonstrating a certain amount of oxygen remains in the graphite carbon after calcination [41]. As shown in Fig. 3e, Co 2p splits into eight peaks, with a $2p_{3/2}$ binding energy of 777.8 eV and a $2p_{1/2}$ binding energy of 794 eV corresponding to metallic cobalt, and the $2p_{3/2}$ binding energy of 779.4 eV and the $2p_{1/2}$ binding energy of 795.6 eV can be assigned to Co^{2+}, the $2p_{3/2}$ binding energy of 781.4 eV and the $2p_{1/2}$ binding energy of 797.1 eV can be identified to Co^{3+}, and accompanied by two additional shake-up satellites [42, 43]. The Ni 2p spectrum has four peaks at 852, 869, 855.1 and 873 eV, which are fitted to the Ni $2p_{3/2}$, Ni $2p_{1/2}$, Ni^{2+} $2p_{3/2}$ and Ni^{2+} $2p_{1/2}$ multiplets and present with two satellites [44, 45]. More details of the high-resolution Co 2p and Ni 2p spectra of CoNi@PC_2–3 are provided in Fig. S1. Each of them has the same chemical composition and valence state of the elements as CoNi@PC_1. The coexistence of Co^{2+}, Co^{3+}, and Ni^{2+} in CoNi@PC_1-3 can be attributed to two causes, the residuals of unreduced metal ions, and the formation of Co_3O_4 and NiO due to the reaction of Co^{2+} and Ni^{2+} with oxygen from the carboxyl group. In summary, it can be inferred that the as prepared bimetallic composites (CoNi@PC) are composed of metallic cobalt, metallic nickel, graphite carbon, Co_3O_4 and NiO.

Raman spectra are used to assess the degree of graphitization of the sample, which have a large impact on the dielectric loss of carbon-based materials. All materials show peaks around 1340 and 1580 cm^{-1} corresponding to the D band and G band, respectively, as shown in Fig. 3f, confirming the presence of amorphous and graphitic carbon [41]. The integrated intensity ratio of the D band and G band (I_D/I_G) reflects the graphitization degree of the composites. The I_D/I_G ratios of Co@PC, Ni@PC, CoNi@PC_1, CoNi@PC_2,

and CoNi@PC_3 is equal to 0.83, 0.84, 0.84, 0.84, and 0.84, indicating that they have the same degree of defects and graphitization due to the same carbon source and calcination temperature.

The magnetic properties of the samples were investigated at room temperature (Fig. 3 g and h). Saturation magnetization (Ms) and coercivity (Hc) are important parameters in evaluating the magnetic properties of materials. All samples exhibit typical ferromagnetic hysteresis loops, which should be attributed to the presence of magnetic Co, Ni or CoNi alloys in the composites. The Ms values of Co@PC and Ni@PC are 71.4 emu/g and 40.69 emu/g, respectively. The Ms value of Co@PC is significantly higher than that of Ni@PC. The saturation magnetization (Ms) values of CoNi@PC_1-3 are 30.2 emu/g, 42.1 emu/g and 64.8 emu/g, respectively, and the Ms value gradually increases with increase the loading ratio of Co/Ni, demonstrating that the ratio of Co and Ni in the alloy have a great influence on the magnetic properties of the materials. The Hc values (Fig. 3h) are 21.43, 164.16, 339.71, 378.48 and 391.70 Oe, corresponding to Ni@PC, CoNi@PC_1, Co@PC, CoNi@PC_3, and CoNi@PC_2, respectively. The increased value of Hc is attributed to the increased of the surface anisotropic field due to the small particle size effect [46, 47]. Generally, a high value of Ms and a low value of Hc are favorable for improving permeability and therefore for enhancing magnetic loss capacity. Both Ni@PC and CoNi@PC_1 have relatively low Hc values, which are largely smaller than the Hc values from the other three samples. Although they do not have higher Ms values, the difference in Ms values is small compared to the difference in Hc values between the Ni@PC or CoNi@PC_1 sample and the other samples. Therefore, for both Ni@PC and CoNi@PC_1 the lower value of Hc provides more influence for enhancing the magnetic loss capacity.

Typical SEM images of samples that calcined in argon are shown in Fig. 4a–e, and their enlarged SEM images are shown in Fig. 4a1–e1. For the heat-treated samples, their external features are roughly maintained similarly to those of the original morphology, with differences present for Co@PC and CoNi@PC_1-3, which are shrunk (Fig. 4a) and crushed to many particles (Fig. 4c–e), respectively. As for Ni@PC (Fig. 4b), many tiny pores and nanospheres appear on the surface of the flower-like structures, which is clearly visible from the enlarged SEM image (Fig. 4b1). SEM images of the respective enlarged fracture profiles for Co@PC and CoNi@PC_1-3 display randomly
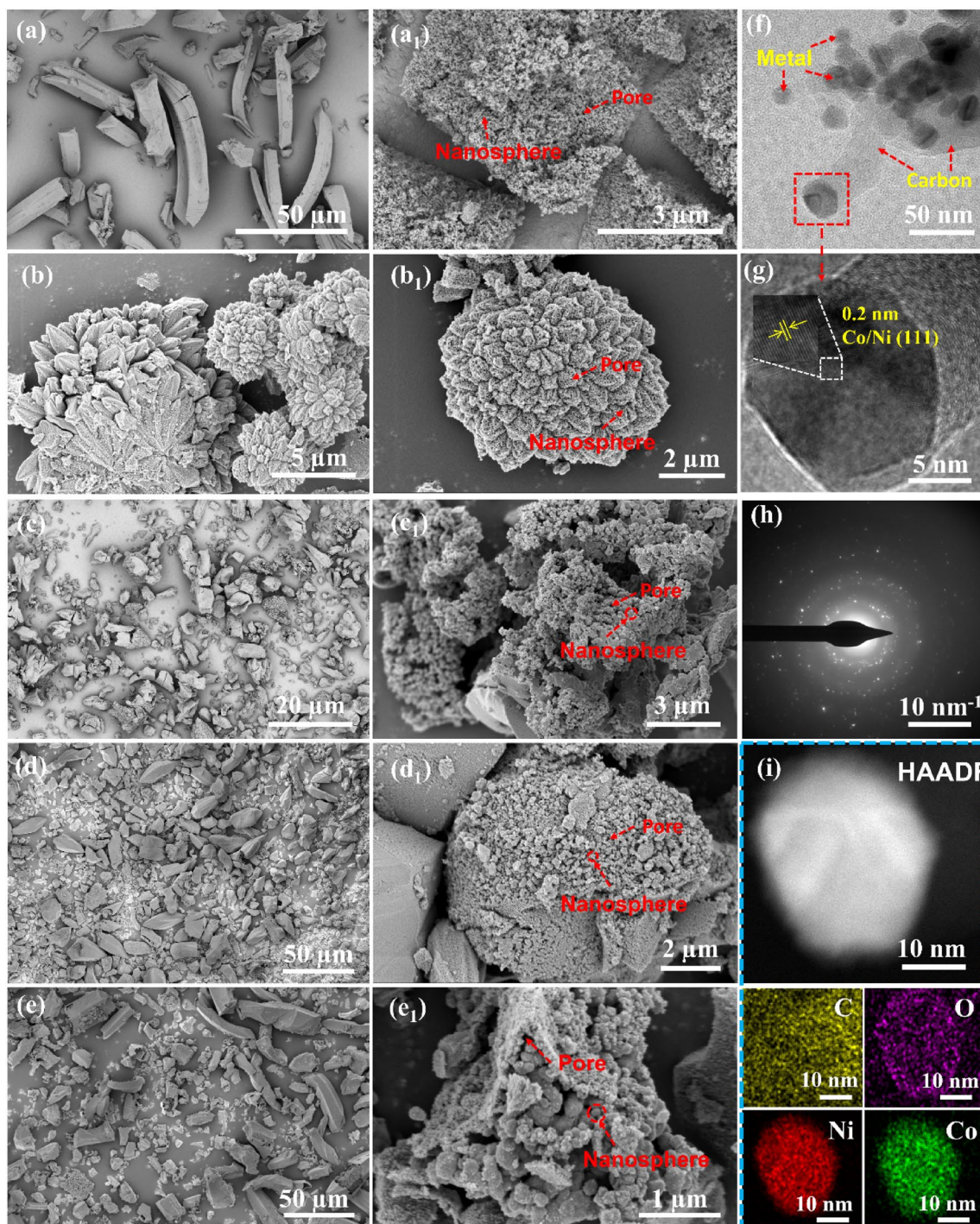
Fig. 4 SEM images of Co@PC (**a**, **a₁**), Ni@PC (**b**, **b₁**), CoNi@PC_1 (**c**, **c₁**), CoNi@PC_2 (**d**, **d₁**), CoNi@PC_3 (**e**, **e₁**) and TEM images (**f**), HR-TEM (**g**), SAED patterns (**h**) and the corresponding elemental mapping spectra of CoNi@PC_1 (**i**)

dispersed nanospheres are presented in the interior of the porous structure (Fig. 4a1 and c1–e1). It can be inferred that the spherical grains compose of carbon, cobalt, nickel and their alloys, the pores may be due to the decomposition of the organic ligands in MOF-74 into CO_2 and H_2O, with the resulting gas facilitating the formation of the porous structure. Overall, the pyrolysis process of MOF-74 at 700 °C in an inert

atmosphere will result in microstructural changes and substance transformation.

Figure 4f-i show the TEM and HR-TEM images of CoNi@PC_1. As displayed in Fig. 4f, the spherical particles of cobalt-nickel alloy are found to scatter inside the carbon to form core-shell structure. In the HR-TEM of nanospheres (Fig. 4g), the lattice fringes with a spacing of 0.2 nm, corresponding well to the (111) planes of the fcc structure of Co/Ni alloy. The selected area electron diffraction (SAED) images (Fig. 4h) showed a series of electron diffraction rings in the carbon-coated CoNi alloy, confirming that the synthesized sample was composed of polycrystalline nanoparticles. Figure 4i show the high-angle annular dark-field (HAADF) and their corresponding elemental mapping spectra of CoNi@PC_1, where it is evident that the C, O, Co, and Ni elements are evenly distributed. It indicates that Co and Ni are dispersed in the carbon matrix, while the pixels density of nickel element is higher than that of cobalt element, which is consistent with the feeding ratio, and it further shows that Co and Ni are involved in fabricating CoNi@PC_1.

3.2 Electromagnetic parameter analysis

According to the electromagnetic energy conversion principle [48, 49], the complex permittivity ($\varepsilon_r = \varepsilon' - j\varepsilon''$) and complex permeability ($\mu_r = \mu' - j\mu''$) of composites are studied to evaluate the attenuation capacity of EMA [50]. The real parts (ε', μ') of the electromagnetic parameters are used to characterize the storage capacity of electromagnetic energy, while the imaginary parts (ε'', μ'') represent the dissipation capacity [51, 52]. The dielectric dissipation factors (tan$\delta\varepsilon = \varepsilon''/\varepsilon'$) and magnetic dissipation factors (tan$\delta\mu = \mu''/\mu'$) are applied to describe the dielectric and magnetic loss abilities and the relationship between energy storage and attenuation of EMA. As shown in Fig. 5a, all samples exhibit a decrease of ε' value with the increase in frequency, which can be attributed to dispersion effect, illustrating the orientation polarization of the electric dipole lagging the periodic variation of the electromagnetic field. This phenomenon favors the absorption of EM wave [37]. As is well-known, a higher ε' value, in the same test frequency, indicates better dielectric storage ability. The dielectric storage capacity relationship among the samples is CoNi@PC_1 > CoNi@PC_2 > Co@PC > Ni@PC > CoNi@PC_3. In detail, the ε' value of Co@PC declines slightly from 6.3 to 5.2, the ε' value of Ni@PC declines from 6.9 to 4.5, the ε' value of CoNi@PC_1 declines from 9.5 to 7.1, the ε' value of CoNi@PC_2 declines from 6.6 to 5.6, and ε' value of CoNi@PC_3 decreases from 4.7 to 3.4. Figure 5b illustrates the imaginary part of the permittivity (ε''>) of all composites. The ε'' values of Ni@PC, CoNi@PC_1 and CoNi@PC_3 show a downward trend of vibration, whereas Co@PC and CoNi@PC_2 have similar ε'' values and increase slightly with increase the frequency. In detail, the ε'' value of Co@PC fluctuates between 1.0 and 1.3, and the ε'' value of CoNi@PC_2 vibration around 1.2, the ε'' value of Ni@PC has dropped from 2.2 to 1.9, the ε'' value of CoNi@PC_1 has dropped from 3.2 to 2.4, and the ε'' value of CoNi@PC_3 decreased from 1.7 to 0.7. The ε' and ε'' value of CoNi@PC_1 is always the largest among the five samples, which is beneficial for producing stronger dielectric loss. Thermal treatment leads to graphitization of organic components, which has the ability to improve the electrical conductivity of the composites and produce defective graphite, resulting in enhanced values of both ε' and ε'' [53]. Meanwhile, the core-shell structure provides an adequate interface between the carbon shell and the metallic cobalt and nickel cores, which accumulates a large number space charges and contributes to the enhancement of the interfacial polarization [37]. However, there are a significant difference in the curve distribution or value variation of ε' and ε'' of the five composites, even though they were synthesized by using the same organic molecules and have the same calcination temperature, which may produce similar defects and conductivity. Thus, the amount of space charge formed by metallic cobalt, nickel, or their alloys with the carbon shells is a major factor in determining their interfacial polarization. Dielectric loss tangent (tan$\delta\varepsilon$) indexes the dielectric loss abilities. Figure 5c shows that the tan$\delta\varepsilon$ values of Co@PC, Ni@PC and CoNi@PC_1-3 composites oscillated from 0.16 to 0.26, 0.34 to 0.44, 0.35 to 0.34, 0.19 to 0.22 and 0.38 to 0.20 in the frequency range of 2–18 GHz, which indicated that Ni@PC composites delivered an enhanced dielectric loss. In the diagram, several resonance peaks appear, indicating the existence of a relaxation process in the prepared material. Generally, the polarization mechanism of absorbers is discussed based on Debye relaxation theory. According to Debye's theory, ε' and ε'' can be expressed as [54–57]:

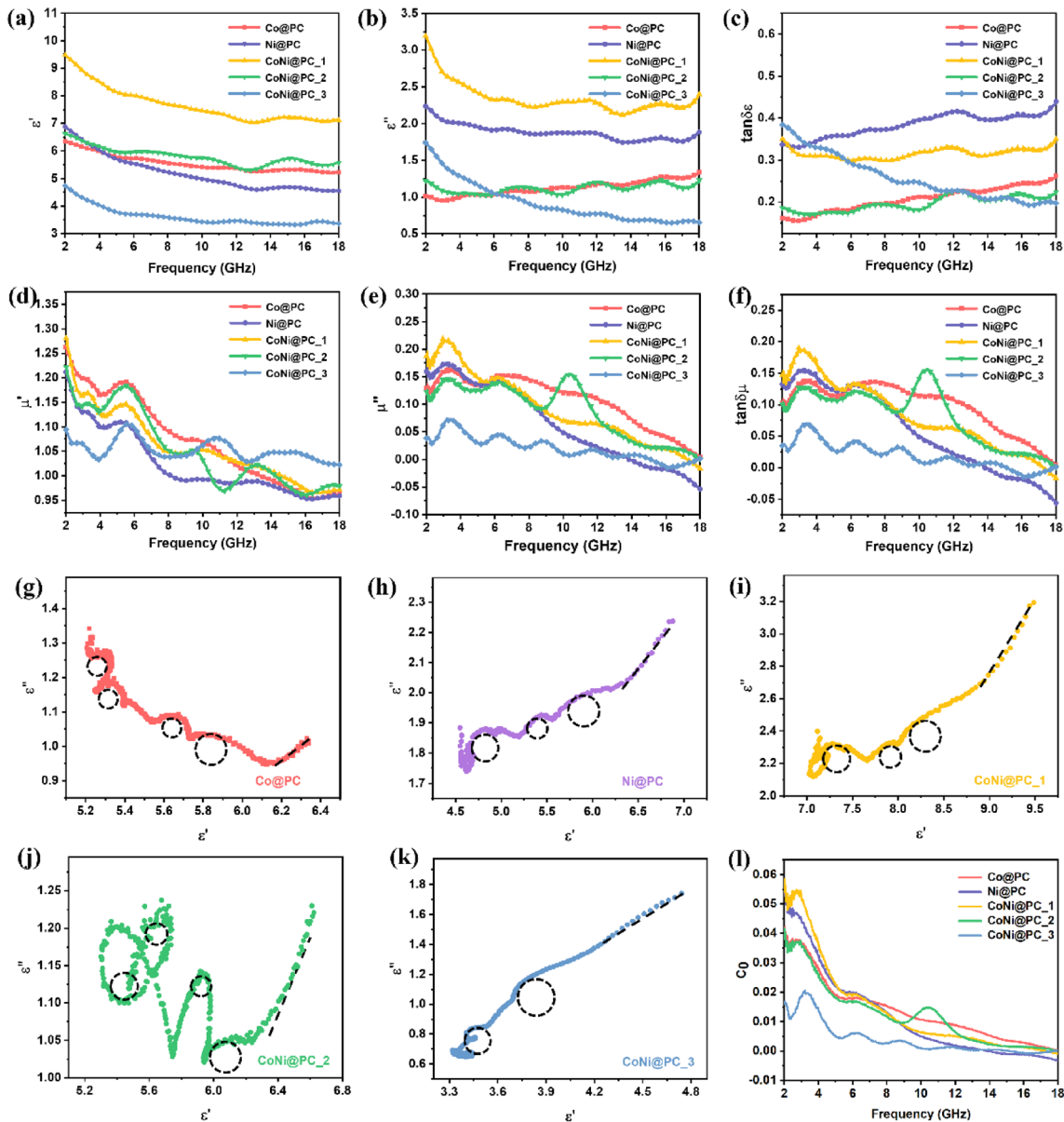$$\varepsilon' = \varepsilon_\infty + \frac{\varepsilon_s - \varepsilon_\infty}{1 + (2\pi f)^2 \tau^2},$$ (1)

Fig. 5 Real permittivity (**a**), imaginary permittivity (**b**), dielectric loss tan δε (**c**), real permeability (**d**), imaginary permeability (**e**), and magnetic loss tan δμ (**f**), Cole–Cole plots (**g–k**) and C_0 curves **l** of Co@PC, Ni@PC, CoNi@PC_1, CoNi@PC_2, and CoNi@PC_3

$$\varepsilon'' = \frac{2\pi f \tau (\varepsilon_s - \varepsilon_\infty)}{1 + (2\pi f)^2 \tau^2}. \tag{2}$$

According to the formula, the relation between ε' and ε'' can be deduced, namely [58, 59]:

$$\left(\varepsilon' - \frac{\varepsilon_s + \varepsilon_\infty}{2}\right)^2 + (\varepsilon'')^2 = \left(\frac{\varepsilon_s - \varepsilon_\infty}{2}\right)^2, \tag{3}$$

where ε_s is the static permittivity, and ε_∞ is the relative permittivity. The ε'' vs. ε' curves are composed of a series of semicircles (Cole–Cole semicircles). Each semicircle represents a Debye relaxation process. As shown in Fig. 5g–k, samples of Co@PC, Ni@PC, CoNi@PC_1, CoNi@PC_2 contain at least two semicircles and one long-tailed straight line, and CoNi@PC_3 only has only one long-tailed straight line. According to Debye theory, semicircular and the long-tailed straight line are associated with polarization relaxation and

conduction loss, respectively. In particular, the numbers of the Cole-Cole semicircles in Co@PC, Ni@PC, CoNi@PC_1, CoNi@PC_2, CoNi@PC_3 are 4, 3, 3, 4, 2 respectively, indicating that they all have polarization and conduction losses [60]. Therefore, the difference in dielectric losses for the five composites is due to the difference in the number of space charges between the metallic core and the carbon shell.

Figure 5d shows that the μ' value of Co@PC, Ni@PC and CoNi@PC_1-3 composites changed from 1.26 to 0.96, 1.21 to 0.96, 1.28 to 0.97, 1.22 to 0.98 and 1.09–1.02, respectively. The μ'' value of Co@PC, Ni@PC and CoNi@PC_1-3 ranged from 0.13 to nearly zero, 0.16 to − 0.05, 0.19 to − 0.02, 0.12 to nearly zero and 0.04 to nearly zero, respectively (Fig. 5e). The complex permeability (μ' and μ'') for all the samples clearly exhibit a similar tendency in 2–18 GHz, which display enhanced storage and dissipation capacity in the low-frequency region. Moreover, all the μ' and μ'' values of composites show obvious fluctuations in 2–18 GHz, indicating that all the samples have magnetic response properties. In addition, according to Maxwell's equations, alternating electric field can generate magnetic field, which can radiate electromagnetic waves, resulting in the negative value of μ'' at high frequency for Ni@PC, which helps to improve its dielectric loss property [35, 61]. Magnetic losses are generally related to a various loss mechanism, namely domain wall resonance, hysteresis loss, eddy current loss, exchange resonance and natural resonance [62]. However, domain wall resonance and hysteresis loss do not participate in the operation at 2–18 GHz frequency. Eddy current loss (C_0) plays an important role in magnetic loss. C_0 can be expressed by the following formula [63, 64]:

$$C_0 = \mu''(\mu')^{-2}f^{-1} = 2\pi\mu_0 d^2\sigma, \tag{4}$$

where μ_0 is the vacuum permeability, d is the sample's thickness, and σ is the electric conductivity, all of which are constant for one sample.

If C_0 is the main contributor to the magnetic loss, C_0 is linear over the frequency range and remains constant in value [65], as depicted in Fig. 5l, all the curves exhibit downward trend, demonstrating no significant eddy current loss occur in the test frequency range. Moreover, the fluctuation of the value in the low frequency region indicates that the magnetic loss are a combination of exchange resonance and natural resonance [66]. Note particularly that both Ni@PC

and CoNi@PC_1 have higher C_0 values in the 2–6 GHz range, indicating a pronounced exchange resonance, as evidenced by their lower Hc values (Fig. 3 g and h). Magnetic loss tangent ($\tan\delta_\mu$) shown in Fig. 5f., standing for the dissipation ability of magnetic energy, has the analogous curve fluctuation with μ'', indicating that the magnetic loss of the samples is mainly attributed to the natural resonance and exchange resonance.

3.3 Electromagnetic wave absorption properties

According to the transmit-line theory [67], the EMA performance of the composites can be evaluated by the reflection loss (RL) value, which can be expressed by the following Eqs. [68, 69]:

$$RL = 20\lg\left|\frac{Z_{in} - Z_0}{Z_{in} + Z_0}\right|, \tag{5}$$

$$Z = \frac{Z_{in}}{Z_0} = \sqrt{\frac{\mu_r}{\varepsilon_r}}\tan h\left(j\frac{2\pi fd}{c}\sqrt{\varepsilon_r\mu_r}\right), \tag{6}$$

where Z_{in} is the input impedance of the absorber, Z_0 is the impedance of free space, d is the thickness of the absorber, f and c are the frequency of electromagnetic wave and the velocity of light, respectively. To meet the demand for practical applications, more than 90% of the microwave should be attenuated, which means that the value of RL should be lower than − 10 dB. Figure 6 shows the maximum reflection loss for Co@PC, Ni@PC and CoNi@PC_1-3 at thicknesses of 1–6 mm. Obviously, Ni@PC, and CoNi@PC_1 have excellent microwave absorption properties, with the minimum reflection loss (RL_min) shifted to the low frequencies with increasing thickness (Fig. 6a2 and a3), and the RL_min values are − 23.21 dB and − 38.7dB at the thickness of 5 and 6 mm, respectively. It can be seen from Fig. 6b2 and c2 that the maximum effective absorption bandwidth (EAB_max) is 4.72 GHz at the matching thickness of 2.66 mm for Ni@PC. The EAB_max is 4.16 GHz at the thickness of 2.08 for CoNi@PC_1 (Fig. 6b3 and c3), it shows similar EAB_max with Ni@PC but exhibits thinner absorption thickness, and its effective absorption ranging at 3.36–18 GHz. However, the other three samples exhibit relatively weak EMA performance, especially for the CoNi@PC_3 composite, where no effective reflection loss can be generated in the test frequency range (Fig. 6a5, b5, c5). The RL_min is − 11.16 dB at 11.28 GHz with a thickness of 2.5 mm, and the
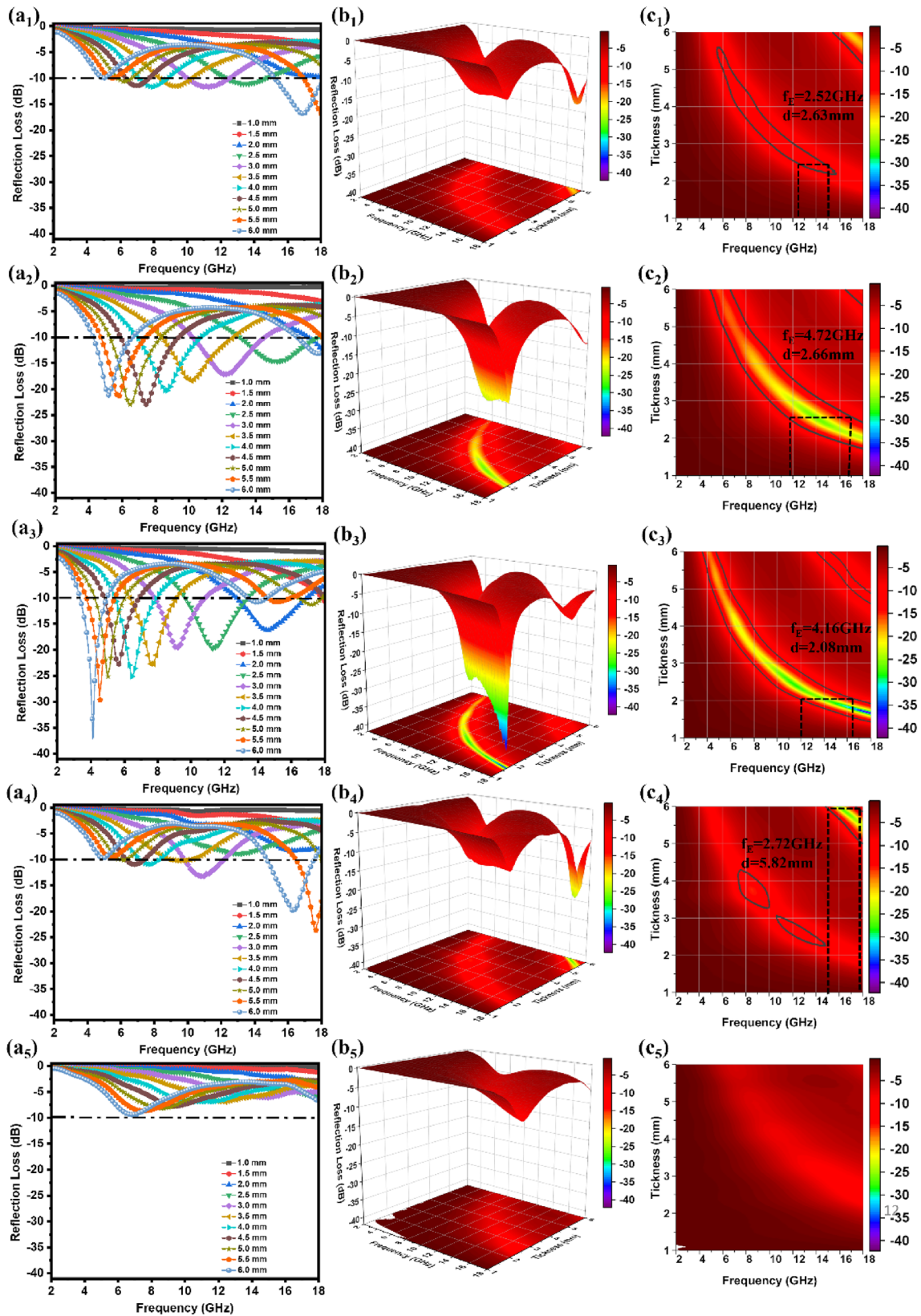
Fig. 6 RL curves (a_1–a_5), 3D RL (b_1–b_5) and EAB (c_1–c_5) values of Co@PC, Ni@PC, CoNi@PC_1, CoNi@PC_2, and CoNi@PC_3

EAB_{max} is 2.52 GHz for Co@PC (Fig. 6a1, b1, c1). The RL_{min} is -23.7 dB at 17.68 GHz with a thickness of 5.5 mm, and the EAB_{max} is 2.72 GHz for CoNi@PC_2 (Fig. 6a4, b4, c4). It can be concluded that the RL properties of the calcined samples are highly dependent on the metal composition of MOF-74 due to the reduced metallic particles or alloys have different magnetic response characteristics. In addition, the carbon shell largely enhances the electrical conductivity, and the porous structure helps to increase the multiple scattering and interfacial polarization, which also play an important role in increasing the EMA performance. Moreover, the tight binding of metallic components and carbon shells generates interfacial polarization, which can greatly facilitate dielectric loss in composites. Whereas, Co, Ni, and CoNi alloys with different ratios will form different interface states with their graphitic carbon components, leading to the differences in the number of spatial charges at the interface, which in turn leads to differences in their dielectric loss capabilities. As a result, the superior EMA performance of Ni@PC and CoNi@PC_1 may be due to the presence of a large amount of space charges at the core-shell interface.

3.4 Microwave absorption mechanism analysis

To clarify the EMA enhancement mechanism of the composites, the impedance matching characteristics and attenuation coefficient (α) were determined. Impedance matching ($|Z_{in}/Z_0|$) is the ratio of input impedance to free space impedance, which is usually utilized to evaluate the degree of incident EM entering the absorber. When the impedance matching value is equal to 1, the incident electromagnetic wave will not be reflected, and the impedance matching characteristics will be the best [70]. The impedance matching of the composites was analyzed at a thickness of 2 mm. As shown in Fig. 7a, by comparison, the relations of the $|Z_{in}/Z_0|$ values are CoNi@PC_3 > CoNi@PC_2 > Co@PC > Ni@PC > CoNi@PC_1 in the range of 10–18 GHz. Nearly all the values of $|Z_{in}/Z_0|$ of CoNi@PC_3 deviate from 1, indicating the poor impedance matching. The values of $|Z_{in}/Z_0|$ for CoNi@PC_1 is closer to 1, indicating that the better impedance matching gives access to the incident wave to the sample, in agreement with the results shown on its RL curve. Thus, the superior impedance matching characteristic of CoNi@PC_1 paves the way for the subsequent attenuation of the incident wave.

To assess the incident EM attenuation ability of the samples, the attenuation constant (α) values of samples are determined by the following formula [71–73]:

$$\alpha = \frac{\sqrt{2}\pi f}{c} \times \sqrt{(\mu''\varepsilon'' - \mu'\varepsilon') + \sqrt{(\mu''\varepsilon'' - \mu'\varepsilon')^2 + (\varepsilon'\mu'' + \varepsilon''\mu')^2}}. \quad (7)$$

As shown in Fig. 7b, all the five samples have a similar variation trend, the values of α gradually increasing with increasing the frequency. The α values of the five samples are as follows: CoNi@PC_1 > Ni@PC > Co@PC > CoNi@PC_2 > CoNi@PC_3. The curves of α and ε'' has the analogous progressive trend ε'' due to their positively correlated function according Eq. (7). As depicted in curves, CoNi@PC_1 has the highest value in the whole frequency range, correlating to the highest ε'' values, illustrating the strongest consumption capability to incident wave.

In general, the superior EMA properties of MOF-derived composites are determined by the calcined products of carbon, metal, or metal oxides, and the specific core-shell microstructure. Based on the above discussion, we can summarize the EMA mechanism diagram of MOF-derived Co/Ni/C nanocomposites (Fig. 8). In short, the ferromagnetic components of

Fig. 7 α value plots (**a**), and $|Z_{in}/Z_0|$ plots (**b**) of all the samples
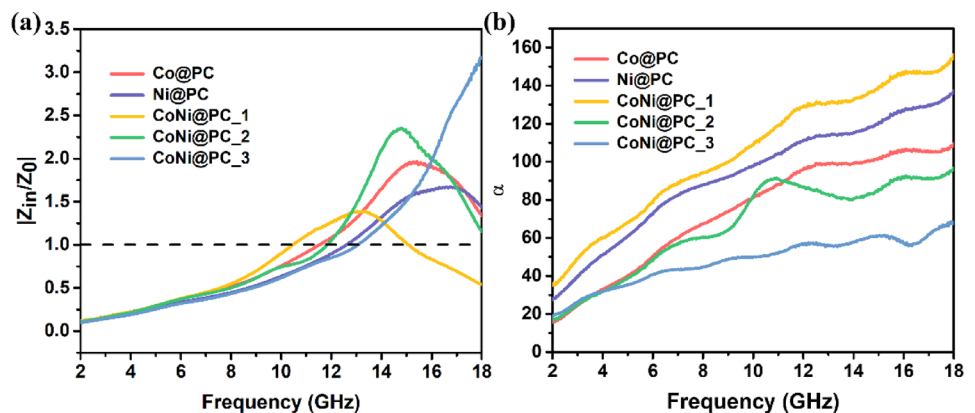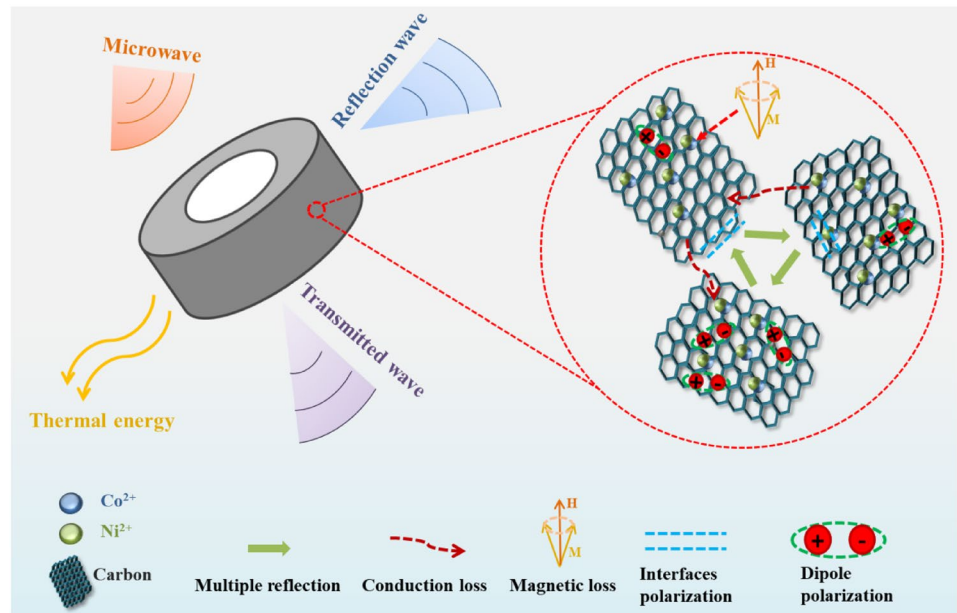
Fig. 8 Schematic diagrams of the potential EMA mechanisms of the composites

the cobalt, nickel or their alloy cores and the dielectric part of the carbon shell are efficiently combined in this work. First, the porous structure give rise to multiple reflections and scatters of the incident electromagnetic wave in the composite, increasing the energy loss during propagation. Second, the carbon shell enhances the electrical conductivity, which facilitates the conduction loss. The core-shell structure between the highly crystalline metallic or metallic alloy core and the carbon shell increases the contact interface and further increases the interfacial polarization. However, differences in the constituent states of metallic substances, resulting in differences in the number of generated space charges, directly affects their interfacial polarization capabilities. Here, the amount of space charge is considered as the primary effect on the dielectric loss properties. Third, the ferromagnetic components of cobalt, nickel and their alloys have a large impact on the magnetic properties, greatly enhancing the magnetic loss and modulating the impedance matching performance. However, the realization of excellent EMA properties of materials is not uniquely determined by a single property, and many factors need to be considered to understand the absorption mechanisms for all samples, including interfacial polarization, conduction loss, dipole polarization, magnetic loss, and impedance matching. It is well known that the impedance matching characteristic is a precondition for the onset of the attenuation of electromagnetic wave, and as described above, the relatively poor

impedance matching of CoNi@PC_3, CoNi@PC_2 and Co@PC leads to the weak EMA performance as fewer electromagnetic waves can enter the composite, even though they have some degree of attenuation capacity. Compared to other composites, Ni@PC and CoNi@PC_1 have superior EMA performance in terms of thin thickness, large effective bandwidth range, and strong absorption intensity due to their good conductivity from the carbon shell, the tight binding of the metallic alloy/carbon and the presence of increased space charges enhance the interfacial polarization, the well-regulated impedance matching between the dielectric/magnetic components, and their better magnetic loss properties.

4 Conclusion

In summary, we have prepared five samples of MOF-74 with metallic clusters of different Co/Ni ionic ratios by hydrothermal method. Then, these as synthesized MOF-74 were treated by one-step in-situ pyrolysis at 700 °C under nitrogen atmosphere. The resulting Co/Ni/C composites derived from MOF-74 exhibit distinct differences in their electromagnetic response absorption properties. Of these, Ni@PC has a better EMA performance, reflected in its broad EAB_{max} of 4.72 GHz at a thickness of 2.66 mm, while the EAB of CoNi@PC_1 achieves an EAB_{max} of 4.16 GHz at a thickness of 2.08 mm, a thinner thickness at a similar absorption width.

Moreover, CoNi@PC_1 also has the strongest absorption intensity at all thicknesses.

In addition to the dielectric loss from carbon, the magnetic loss from cobalt, nickel or their alloys and porous structure, the space charges formed between the magnetic core and the dielectric carbon shell largely affect their dielectric loss of the interfacial polarization, and the optimal impedance matching is also the key factor to determine the EMA performance of the CoNi@PC_1 composite. The synthesis of the bimetallic MOF-74 with adjustable metal ions ratio offers a new idea to explore more promising materials for electromagnetic wave absorption. Combined with the simple fabrication method, MOF-74 derived composites provide a high utilization value for electromagnetic pollution in practical application.

Author contributions

All authors contributed to the study conception and design. Material preparation, data collection and analysis were performed by YL, KZ. The first draft of the manuscript was written by YL, KZ and all authors commented on previous versions of the manuscript. All authors read and approved the final manuscript. YL and KZ contributed equally to this work.

Funding

Data availability

All data included in this study are available upon request by contact with the corresponding author.

Declarations

Conflict of interest The authors have no relevant financial or non-financial interests to disclose.

Supplementary Information The online version contains supplementary material available at https://doi.org/10.1007/s10854-023-11640-y.

References

1. Y. Cui, K. Yang, J. Wang, T. Shah, Q. Zhang, B. Zhang, Carbon **172**, 1 (2021)
2. X. Zhou, Z. Jia, A. Feng, J. Kou, H. Cao, X. Liu, G. Wu, Compos. Part B Eng. **192**, 107980 (2020)
3. X. Yang, X. Zhong, J. Zhang, J. Gu, J Mater Sci Technol. **68**, 209 (2021)
4. M.-S. Cao, X.-X. Wang, W.-Q. Cao, J. Yuan, J. Mater. Chem. C **3**, 6589 (2015)
5. D.D.L. Chung, Carbon **39**, 279 (2001)
6. S. Geetha, K.K. Satheesh Kumar, C.R.K. Rao, M. Vijayan, D.C. Trivedi, J Appl. Polym. Sci. **112**, 2073 (2009)
7. F. Qin, C. Brosseau, J. Appl. Phys. **111**, 061301 (2012)
8. A.N. Yusoff, M.H. Abdullah, S.H. Ahmad, S.F. Jusoh, A.A. Mansor, S.A.A. Hamid, J. Appl. Phys. **92**, 876 (2002)
9. J.-M. Thomassin, C. Jérôme, T. Pardoen, C. Bailly, I. Huynen, C. Detrembleur, Mater. Sci. Eng. R Rep. **74**, 211 (2013)
10. J. Joo, C.Y. Lee, J. Appl. Phys. **88**, 513 (2000)
11. S. Motojima, Y. Noda, S. Hoshiya, Y. Hishikawa, J. Appl. Phys. **94**, 2325 (2003)
12. A. Wang, W. Wang, C. Long, W. Li, J. Guan, H. Gu, G. Xu, J. Mater. Chem. C **2**, 3769 (2014)
13. X. Huang, J. Zhang, M. Lai, T. Sang, J. Alloys Compd. **627**, 367 (2015)
14. X. Wu, S. Chen, Y. Feng, Q. Yuan, J. Gao, Y. Chen, Y. Huang, Y.-B. He, W. Gan, Mater. Today Phys. **9**, 100132 (2019)
15. J. Zhao, J. Zhang, L. Wang, J. Li, T. Feng, J. Fan, L. Chen, J. Gu, Compos. Commun. **22**, 100486 (2020)
16. Z. Wang, X. Li, L. Wang, Y. Li, J. Qin, P. Xie, Y. Qu, K. Sun, R. Fan, Adv. Compos. Hybrid. Mater. **3**, 1 (2020)
17. J. Yu, Y. Li, X. Xu, G. Duan, Y. Li, W. Zhou, Compos. Commun. **24**, 100643 (2021)
18. D. Liu, Y. Du, F. Wang, Y. Wang, L. Cui, H. Zhao, X. Han, Carbon **157**, 478 (2020)
19. L. Wang, X. Shi, J. Zhang, Y. Zhang, J. Gu, J. Mater. Sci. Technol. **52**, 119 (2020)

20. P. Liu, S. Gao, Y. Wang, F. Zhou, Y. Huang, J. Luo, Compos. Part B Eng. **202**, 108406 (2020)

21. Y. Lian, B. Han, D. Liu, Y. Wang, H. Zhao, P. Xu, X. Han, Y. Du, Nano-Micro Lett. **12**, 153 (2020)

22. T. Hou, J. Wang, T. Zheng, Y. Liu, G. Wu, P. Yin, Small (2023). https://doi.org/10.1002/smll.202303463

23. P. Yi, X. Zhang, L. Jin, P. Chen, J. Tao, J. Zhou, Z. Yao, Chem. Eng. J **430**, 132879 (2022)

24. H. Peng, M. He, Y. Zhou, Z. Song, Y. Wang, S. Feng, X. Chen, X. Zhang, H. Chen, Chem. Eng. J. **433**, 133269 (2022)

25. Z. Li, X. Han, Y. Ma, D. Liu, Y. Wang, P. Xu, C. Li, Y. Du, ACS Sustain. Chem. Eng. **6**, 8904 (2018)

26. J. Zhou, D. Lan, F. Zhang, Y. Cheng, Z. Jia, G. Wu, P. Yin, Small (2023). https://doi.org/10.1002/smll.202304932

27. J.-K. Sun, Q. Xu, Energy Environ. Sci. **7**, 2071 (2014)

28. F. Zhang, Z. Jia, J. Zhou, J. Liu, G. Wu, P. Yin, Chem. Eng. J. **450**, 138205 (2022)

29. P. Yin, G. Wu, Y. Tang, S. Liu, Y. Zhang, G. Bu, J. Dai, Y. Zhao, Y. Liu, Chem. Eng. J. **446**, 136975 (2022)

30. B.W. Jacobs, R.J.T. Houk, M.R. Anstey, S.D. House, I.M. Robertson, A.A. Talin, M.D. Allendorf, Chem. Sci. **2**, 411 (2011)

31. L. Peng, J. Zhang, Z. Xue, B. Han, J. Li, G. Yang, Chem. Commun. **49**, 11695 (2013)

32. P. Gai, H. Zhang, Y. Zhang, W. Liu, G. Zhu, X. Zhang, J. Chen, J. Mater. Chem. B **1**, 2742 (2013)

33. K.E. deKrafft, C. Wang, W. Lin, Adv. Mater. **24**, 2014 (2012)

34. B. Liu, H. Shioyama, T. Akita, Q. Xu, J. Am. Chem. Soc. **130**, 5390 (2008)

35. L. Ma, S. Li, F. Liu, S. Ma, E.-H. Han, Z. Zhang, J. Alloys Compd **906**, 164257 (2022)

36. B. Wen, H. Yang, Y. Lin, L. Wang, L. Ma, Y. Qiu, Compos. Part. Appl. Sci. Manuf. **138**, 106044 (2020)

37. K. Wang, Y. Chen, R. Tian, H. Li, Y. Zhou, H. Duan, H. Liu, ACS Appl. Mater. Interfaces **10**, 11333 (2018)

38. J. Ouyang, Z. He, Y. Zhang, H. Yang, Q. Zhao, ACS Appl. Mater. Interfaces **11**, 39304 (2019)

39. P. Xue, Y. Chen, Y. Xu, C. Valenzuela, X. Zhang, H.K. Bisoyi, X. Yang, L. Wang, X. Xu, Q. Li, Nano-Micro Lett. **15**, 1 (2023)

40. X. Zhang, X. Tian, C. Liu, J. Qiao, W. Liu, J. Liu, Z. Zeng, Carbon **194**, 257 (2022)

41. X. Yang, S. Fan, Y. Li, Y. Guo, Y. Li, K. Ruan, S. Zhang, J. Zhang, J. Kong, J. Gu, Compos. Part. Appl. Sci. Manuf. **128**, 105670 (2020)

42. X. Li, A.I. Rykov, B. Zhang, Y. Zhang, J. Wang, Catal. Sci. Technol. **6**, 7486 (2016)

43. G. Sun, H. Wu, Q. Liao, Y. Zhang, Nano Res. **11**, 2689 (2018)

44. M. Fu, Q. Jiao, Y. Zhao, H. Li, J. Mater. Chem. A **2**, 735 (2013)

45. H. Ning, G. Li, Y. Chen, K. Zhang, Z. Gong, R. Nie, W. Hu, Q. Xia, ACS Appl. Mater. Interfaces **11**, 1957 (2019)

46. J. Li, P. Miao, K.-J. Chen, J. Cao, J. Liang, Y. Tang, J. Kong, Compos. Part B Eng. **182**, 107613 (2020)

47. F.L. Jia, L.Z. Zhang, X.Y. Shang, Y. Yang, Adv Mater. **20**, 1050 (2008)

48. I. Abdalla, A. Salim, M. Zhu, J. Yu, Z. Li, B. Ding, ACS Appl. Mater. Interfaces **10**, 44561 (2018)

49. K. Yue, Y. Bo, M.A. Tian, C. Zeng-Yong, Z. Zheng-Jun, J. Inorg. Mater. **33**, 1259 (2018)

50. Y. Wu, D. Lan, J. Ren, S. Zhang, Mater. Today Phys. **36**, 101178 (2023)

51. C. Luo, T. Jiao, J. Gu, Y. Tang, J. Kong, ACS Appl. Mater. Interfaces **10**, 39307 (2018)

52. Y. Zhang, Y. Huang, T. Zhang, H. Chang, P. Xiao, H. Chen, Z. Huang, Y. Chen, Adv. Mater. **27**, 2049 (2015)

53. P. Xu, X. Han, C. Wang, D. Zhou, Z. Lv, A. Wen, X. Wang, B. Zhang, J. Phys. Chem. B **112**, 10443 (2008)

54. F. Pan, L. Yu, Z. Xiang, Z. Liu, B. Deng, E. Cui, Z. Shi, X. Li, W. Lu, Carbon **172**, 506 (2021)

55. M. Zhou, W. Gu, G. Wang, J. Zheng, C. Pei, F. Fan, G. Ji, J. Mater. Chem. A **8**, 24267 (2020)

56. L. Yang, L. Yin, C. Hong, S. Dong, C. Liu, X. Zhang, J. Colloid Interface Sci. **582**, 270 (2021)

57. H. Zhang, K. Sun, K. Sun, L. Chen, G. Wu, J. Mater. Sci. Technol. **158**, 242 (2023)

58. Y. Shi, L. Yu, K. Li, S. Li, Y. Dong, Y. Zhu, Y. Fu, F. Meng, Compos. Sci. Technol. **197**, 108246 (2020)

59. Y. Wei, H. Liu, S. Liu, M. Zhang, Y. Shi, J. Zhang, L. Zhang, C. Gong, Compos. Commun. **9**, 70 (2018)

60. W. Liu, S. Tan, Z. Yang, G. Ji, Carbon **138**, 143 (2018)

61. P. Liu, S. Gao, Y. Wang, Y. Huang, Y. Wang, J. Luo, ACS Appl. Mater. Interfaces **11**, 25624 (2019)

62. P.J. Van Der Zaag, J. Magn. Magn. Mater. **196–197**, 315 (1999)

63. R. Shu, J. Zhang, C. Guo, Y. Wu, Z. Wan, J. Shi, Y. Liu, M. Zheng, Chem. Eng. J. **384**, 123266 (2020)

64. Z. Xu, Y. Du, D. Liu, Y. Wang, W. Ma, Y. Wang, P. Xu, X. Han, ACS Appl. Mater. Interfaces **11**, 4268 (2019)

65. H. Wu, J. Liu, H. Liang, D. Zang, Chem. Eng. J. **393**, 124743 (2020)

66. W. Li, L. Wang, G. Li, Y. Xu, J. Magn. Magn. Mater. **377**, 259 (2015)

67. C. Luo, Y. Tang, T. Jiao, J. Kong, ACS Appl. Mater. Interfaces **10**, 28051 (2018)

68. Y. Pan, Q. Zhu, J. Zhu, Y. Cheng, B. Yu, Z. Jia, G. Wu, Nano Res. **16**, 10666 (2023)

69. S. Zhang, X. Liu, C. Jia, Z. Sun, H. Jiang, Z. Jia, G. Wu, Nano-Micro Lett. **15**, 204 (2023)

70. J. Peng, Z. Peng, Z. Zhu, R. Augustine, M.M. Mahmoud, H. Tang, M. Rao, Y. Zhang, G. Li, T. Jiang, Ceram Int. **44**, 21015 (2018)

71. Z. Yang, H. Lv, R. Wu, Nano Res. **9**, 3671 (2016)

72. L. Huang, C. Chen, X. Huang, S. Ruan, Y.-J. Zeng, Compos. Part B Eng. **164**, 583 (2019)

73. D. Lan, Y. Wang, Y. Wang, X. Zhu, H. Li, X. Guo, J. Ren, Z. Guo, G. Wu, J. Colloid Interface Sci. **651**, 494 (2023)